Title

Ultrafast high-energy micro-supercapacitors based on open-shell polymer-graphene composites

Journal

Cell Reports Physical Science, 3(3)

ISSN

2666-3864

Authors

Yao, Lulu
Liu, Jiaxi
Eedugurala, Naresh
et al.

Publication Date

2022-03-01

DOI

10.1016/j.xcrp.2022.100792

Peer reviewed

Cell Reports
Physical Science

CellPress
OPEN ACCESS

Article

Ultrafast high-energy micro-supercapacitors based on open-shell polymer-graphene composites

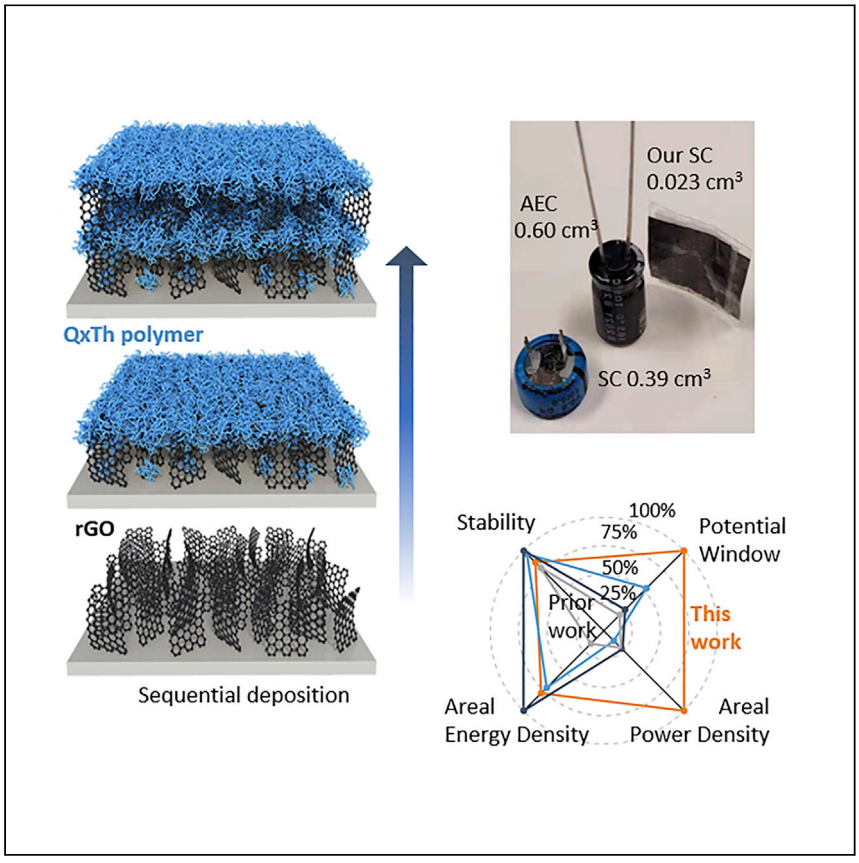

Micro-supercapacitors are promising for on-chip power sources. Yao et al. show that the electro-polymerization of an open-shell conjugated polymer with reduced graphene oxide enables hierarchical electrodes for micro-supercapacitors, simultaneously increasing their power, energy, and lifetime for wireless electronic applications.

Lulu Yao, Jiaxi Liu, Naresh Eedugurala, ..., Kevin S. Mayer, Jason D. Azoulay, Tse Nga Ng

tnn046@ucsd.edu

Highlights

A new class of open-shell conjugated polymer-based composite electrodes

Electrodes incorporating polymers with extended delocalization facilitating 3 V redox stability window

Ultrafast kinetics compatible with a typical AC line frequency of 60 Hz

Suitable replacement for bulky electrolytic capacitors, reducing volume by >10 times

Yao et al., Cell Reports Physical Science 3, 100792
March 16, 2022
https://doi.org/10.1016/j.xcrp.2022.100792

Please cite this article in press as: Yao et al., Ultrafast high-energy micro-supercapacitors based on open-shell polymer-graphene composites, Cell Reports Physical Science (2022), https://doi.org/10.1016/j.xcrp.2022.100792

Cell Reports
Physical Science

Article

Ultrafast high-energy micro-supercapacitors based on open-shell polymer-graphene composites

Lulu Yao,[1] Jiaxi Liu,[2] Naresh Eedugurala,[3] Paramasivam Mahalingavelar,[3] Daniel J. Adams,[3] Kaiping Wang,[1] Kevin S. Mayer,[3] Jason D. Azoulay,[3] and Tse Nga Ng[1,2,4,*]

SUMMARY

Micro-supercapacitors are poised to serve as on-chip power sources for electronics. However, the challenge to simultaneously increase their power, energy, and lifetime demands new material combinations beyond current carbon-based systems. Here, we demonstrate that electro-deposition of an open-shell conjugated polymer with reduced graphene oxide achieves electrodes with capacitance up to 186 mF cm^{-2} (372 F cm^{-3}). The extended delocalization within the open-shell polymer stabilizes redox states and facilitates a 3 V wide potential window, while the hierarchical electrode structure promotes ultrafast kinetics. The micro-supercapacitor shows a high power density of 227 mW cm^{-2} with an energy density of 10.5 μWh cm^{-2} and stability of 84% capacitance retention after 11,000 cycles. These attributes allow operation at 120 Hz for fast charging and alternating current (AC) line filtering applications, which may be suitable to replace bulky electrolytic capacitors or serve as high-endurance energy storage for wireless electronics.

INTRODUCTION

The ultimate goal of electrochemical energy storage technologies is to realize high power and energy density along with stability that spans thousands of charge-discharge cycles.[1–3] Current devices are hampered by trade-offs in their power, energy, and cycling stability. For example, the volumetric energy density of batteries exceeds that of electrochemical supercapacitors and electrolytic capacitors; however, the device power rating, frequency response, and cycle life follow an opposite trend. Currently most batteries and supercapacitors operate below 1 Hz, with slow kinetics that impede their application in alternating current (AC) circuits. A long-standing goal for supercapacitors is to synergistically increase the energy density toward the level achieved by batteries, and concurrently raise the power delivery to match electrolytic capacitors that operate at a typical AC line frequency of 60 Hz.[4,5] If these targets are met, supercapacitors will enable compact power circuits that are not presently achievable owing to the bulky size and weight of electrolytic capacitors. The realization of these supercapacitors will also provide energy storage platforms with much longer cycle lives than batteries, thereby reducing the replacement and maintenance costs of sensor networks.[6,7]

Research on supercapacitors has built upon hierarchical electrode structures[8–15] that promote increases to the device capacitance C and potential window V, since the energy capacity follows from $E = CV^2/2$. One approach to raise the electrode capacitance is to increase the areal loading of active materials; however, thicker electrodes are generally restricted by slow charge-transfer kinetics, which reduce the overall power density within

[1]Materials Science Engineering Program, University of California San Diego, La Jolla, CA 92093, USA

[2]Department of Electrical and Computer Engineering, University of California San Diego, La Jolla, CA 92093, USA

[3]Center for Optoelectronic Materials and Devices, The University of Southern Mississippi, Hattiesburg, MS 39406, USA

[4]Lead contact

*Correspondence: tnn046@ucsd.edu

https://doi.org/10.1016/j.xcrp.2022.100792

Please cite this article in press as: Yao et al., Ultrafast high-energy micro-supercapacitors based on open-shell polymer-graphene composites, Cell Reports Physical Science (2022), https://doi.org/10.1016/j.xcrp.2022.100792

devices. Another method to improve performance is to use redox-active materials such as metal oxides, MXenes, and conducting polymers that raise *C*. However, redox electrodes composed of these materials remain constrained to a potential window $\leq$2 V and exhibit lower cycle lifetimes than electric double-layer capacitors.[1,3] Thus, new materials remain critical to achieve increased energy, power, and lifetime targets.

Here, we describe a hierarchically structured electrode composed of a novel open-shell redox polymer and reduced graphene oxide (rGO)[16–18] that offers state-of-the-art capacitance, an extended potential window, and excellent kinetics and cycle life. Traditionally, π-conjugated materials such as small molecules, polymers, and particularly open-shell species utilized for energy storage applications are unstable on account of the highly localized nature of reduced species and localized radical sites.[19,20] Recently, new classes of donor-acceptor (DA) conjugated polymers[21,22] have been reported that demonstrate significant electronic correlations within the π-conjugated backbone, very narrow bandgaps, open-shell ground states, and intrinsic electrical conductivity. The high degree of electronic coherence promotes extensive delocalization, which serves to thermodynamically stabilize unpaired spins and the resultant charged species. When applied in supercapacitors, this new class of redox-active polymer enabled an increase in the potential window to 3 V, but remained limited in specific capacitance on account of inert solubilizing side chains that are required for solution processing. This structural feature reduced the energy density and power output of thick films in a similar manner to other kinetically limited materials.

To overcome these drawbacks, we demonstrate an electro-polymerization methodology that proceeds directly from the constituent monomers and results in open-shell DA conjugated polymers that are unencumbered by inert solubilizing groups. The open-shell polymers are co-deposited with reduced graphene oxide (rGO) to form porous, conductive scaffolds that result in micrometer-thick electrodes with fast kinetics. The electro-polymerization process is facile, occurs at room temperature, and is amenable to direct integration on silicon chips, so as to enable the fabrication of micro-supercapacitors on integrated circuits for system miniaturization. The process is scalable to large areas enabling high-capacity devices.

Variations in the open-shell polymer-rGO composites are examined to decouple the trade-off between device power and energy density. We further analyze the impact of compositional changes on electrochemical kinetics through equivalent circuit models of the electrodes. Characterization of the devices over 100,000 charge-discharge cycles demonstrates exceptional stability, on account of the unique electronic delocalization of redox states and flexible mechanical framework that tolerates expansion and contraction during redox cycling. The compact, flexible supercapacitors operate at 120 Hz, suitable for AC filtering,[5,23] and are also compatible with pulse and fast charging, which demonstrates their potential to replace bulky electrolytic capacitors in power electronics. In another use case, we integrate the composite device as the sole energy storage component within a wireless energy harvesting system, which enables autonomous short-range electronics.[24,25] This report demonstrates a new generation of redox supercapacitors that enable ultrafast, energy-dense storage with unprecedented cycling durability, and that offers practical utility within emerging microelectronic technologies.

RESULTS AND DISCUSSION

Electrode composition and morphology

In prior works,[21,26–29] redox polymers were synthesized and purified in preparation for a separate deposition step, thus solubilizing groups were required to enable re-dissolution

Please cite this article in press as: Yao et al., Ultrafast high-energy micro-supercapacitors based on open-shell polymer-graphene composites, Cell Reports Physical Science (2022), https://doi.org/10.1016/j.xcrp.2022.100792

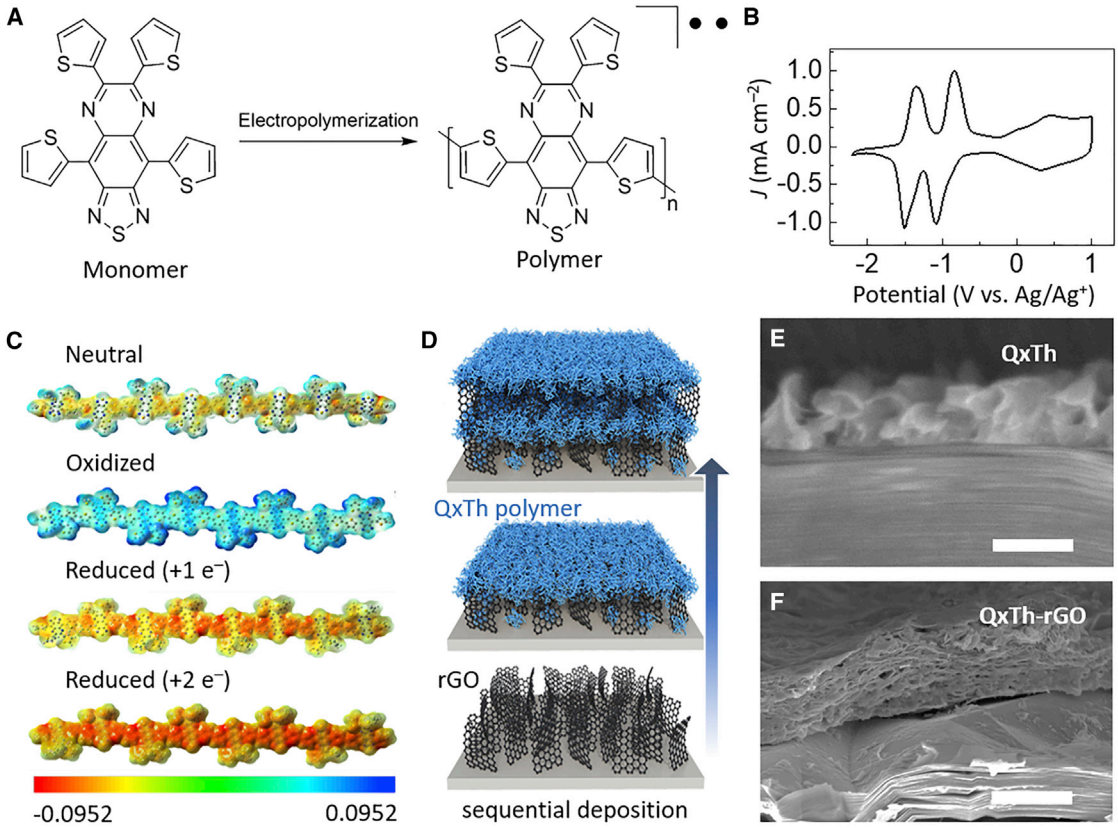

Figure 1. Electrode materials and film formation

(A) Chemical structures of the QxTh monomer and polymer.

(B) CV of the QxTh polymer at a scan rate of 0.1 V s^{-1}.

(C) Molecular electrostatic surface potential (MESP) plots of the polymer in the neutral, oxidized, and reduced (*+1e*$^-$ and *+2e*$^-$) states at $n = 8$. The total electron density is plotted with an isovalue of 0.001 au. The positive (less electrons), neutral, and negative (more electrons) electrostatic regions are indicated by blue, green, and red surfaces respectively.

(D–F) (D) Schematics of the electro-polymerization process to deposit QxTh and rGO in an alternating manner. Cross-sectional SEM images of (E) QxTh polymer and (F) QxTh-rGO composite, with a scale bar representing 300 nm and 5 μm, respectively.

for coating onto substrates. The inert solubilizing groups add mass but do not contribute to the redox activities, lowering the specific capacitance of the materials. This motivated our development of poly(4,6,7,9-tetra(thiophen-2-yl)-[1,2,5]thiadiazolo[3,4-*g*]quinoxaline, an open-shell polymer composed of alternating bithiophene donors and thiophene substituted thiadiazoloquinoxaline acceptors that could be synthesized using an electropolymerization approach. As shown in Figure 1A, the polymerization was carried out by suspending graphite foil electrodes in a mixed solvent of dichloromethane and propylene carbonate containing the monomer 4,6,7,9-tetra(thiophen-2-yl)-[1,2,5]thiadiazolo[3,4-*g*]quinoxaline (QxTh) and 0.1 M tetrabutylammonium hexafluorophosphate ($TBAPF_6$). The electro-polymerized films were used as grown, without additional purification steps. The polymer demonstrated good adhesion to the graphite foil that served as the current collector in supercapacitor devices (Figures S1–S3). The application of potentials higher than 0.5 V (versus Ag/Ag^+) resulted in the growth and deposition of polymer on the graphite foil. Measurements by matrix-assisted laser desorption ionization time of flight mass spectrometry (MALDI-TOF MS; Figure S4) pointed to the formation of the structure depicted in Figure 1A. MALDI-TOF indicated the formation of polymers with up to 12 repeat units (n) using these conditions, indicating the formation of polymers with long conjugation lengths.

Please cite this article in press as: Yao et al., Ultrafast high-energy micro-supercapacitors based on open-shell polymer-graphene composites, Cell Reports Physical Science (2022), https://doi.org/10.1016/j.xcrp.2022.100792

Our electro-polymerization process eliminated the need for inert solubilizing groups, thereby increasing the specific capacitance of the polymeric material. Cyclic voltammetry (CV) (Figures S1C–S1E) was consistent with this point, demonstrating a specific capacitance of 297.6 F g^{-1} between −0.5 V and −2 V (versus Ag/Ag^+), which is a 200% increase over previous generations of n-dopable conjugated polymers.[21,26,27] The CV in Figure 1B also showed that the polymer was stable to −2.2 V (versus Ag/Ag^+), a noteworthy attribute since the majority of n-type polymers are not stable at these low potentials.[30–32] Our polymer, composed of alternating donor and acceptor heterocycles, promotes significant internal charge-transfer characteristics and extended delocalization of unpaired electrons and redox states, resulting in enhanced stability. Overall, the oxidation and reduction reactions of the polymer were reversible over a wide potential window of 3 V, facilitating high-voltage storage that increased the energy densities of our supercapacitors.

Most pseudo-capacitive devices operate within a potential window smaller than 2 V. A primary reason is that many require aqueous electrolytes, in which the water-splitting reaction limits the operational voltage. However, electrode degradation is also an important limiting factor, since most pseudo-capacitive materials provide high redox capacitance only within a small potential window. Their potential windows are normally between −1 V and 1 V versus Ag/Ag^+ reference, so as to limit irreversible reactions and severe degradation of the electrodes. There is a lack of redox materials that are stable in more negative potential range to utilize the full stability window of organic electrolytes, which can be generally safe to operate down to −2 V relative to Ag/Ag^+. Our QxTh-rGO redox composite fills in this gap, providing stable n-dopable electrodes that can be used as anodes together with other cathodes.

The polymer showed linear current-voltage (*I-V*) characteristics with conductivity $\sigma_{RT} \sim 10^{-4}$ S cm^{-1} (Figure S1F). The transport properties can be associated with the narrow bandgap of the polymer, which promote a low energetic barrier for thermal excitation of free carriers and extensive delocalization.[22] At room temperature, continuous-wave electron paramagnetic resonance (EPR) spectroscopy showed a broad single line 2–5 Gauss wide with a *g* factor of 2.0035 (Figure S1G), indicative of the open-shell nature of the polymer. Density functional theory (DFT) calculations at the unrestricted (U)B3LYP/6-31G** level of theory were carried out on oligomers with an increasing number of repeat units and show a rapid transition to an open-shell ground state at chain lengths of $n = 6$. A diradical character index (y) of 0.009 and 0.039 was obtained for the $n = 6$ and 8 oligomers respectively and accounts for the signal and spin concentration obtained by EPR. Molecular electrostatic surface potential (MESP) plots of the $n = 8$ oligomer in the neutral, oxidized, and reduced states ($+1e^-$ and $+2e^-$, respectively) are shown in Figure 1C. These calculations demonstrate that the spin density is distributed throughout the conjugated backbone in the neutral state. When the polymer is oxidized or reduced, charge density is delocalized throughout the π-conjugated backbone, which contrasts with other radical redox polymers where unpaired charge is located on specific radical functional groups. Furthermore, the addition or removal of an electron from the polymer serves to enhance the planarity of the π-conjugated skeleton (Figures S21 and S22), and this high degree of charge delocalization is likely to enhance the stability of different redox states.

Cross-sectional scanning electron microscopy (SEM) images of the electro-polymerized polymer film display a porous morphology (Figures 1E and S1H–S1J) that is advantageous for electrolyte penetration. However, as the polymer thickness was increased, the film became more resistive, limiting further growth. To retain the

Please cite this article in press as: Yao et al., Ultrafast high-energy micro-supercapacitors based on open-shell polymer-graphene composites, Cell Reports Physical Science (2022), https://doi.org/10.1016/j.xcrp.2022.100792

porous structure while improving the overall conductivity of the electrodes, we adjusted the electro-deposition process to incorporate rGO as the conductive matrix. The co-deposition of the polymer-rGO composites onto graphite foils was accomplished by dispersing graphene oxide (GO) flakes within the monomer solution and applying a bias of −2 V for a period of 5 s to reduce the GO into conductive rGO (Figure S3). After this time, the monomers QxTh were polymerized by sweeping the electrode bias at 50 mV s^{-1} from its negative state to 0.8 V and then back to its open-circuit state; this serves as a single deposition cycle (Figure 1D). This sequential deposition of the polymer and rGO resulted in a porous composite (Figures 1F and S3J–S3L) in which the polymer contributes to the high specific capacitance, while rGO provided highly conductive pathways, overcoming the restrictions imposed by the electrical resistance of the neat polymer film. The deposition was carried out up to 3,000 cycles, resulting in a film that is approximately 5 μm thick (Figure S5B). This electro-polymerization process allows the direct deposition of thick films to increase mass loadings per unit area. Furthermore, the process is scalable in area and the composite could be directly integrated on a large (3 × 6 cm) graphite foil (Figure S5E).

Electrochemical characteristics analyzed with equivalent circuit models

We varied the composition of the electro-deposition solution to examine the effects of the polymer-to-rGO ratio on electrode properties. Electrodes of different composition were prepared by varying the concentrations of monomer and GO in the polymerization solution at either 1:1 or 1:5. Figure 2A shows the increase in electrode areal capacitance with deposition cycles, which demonstrates that adding GO raised the deposition efficiency per cycle. We anticipate that incorporating rGO provided additional nucleation sites for the polymerization process, so larger amounts of polymer were deposited when GO was present in the mixture. The 1:1 and 1:5 composite electrodes were nearly comparable in their capacitance. Changing the amount of rGO incorporated into the polymer-rGO composite yielded only a small effect on the electrode capacitance. The gravimetric capacitance of rGO (typically 80–200 F g^{-1})[33] was smaller than the QxTh polymer (298 F g^{-1}). A large portion of the capacitance contribution was due to redox charge exchange in QxTh, and thus we did not raise the GO concentration beyond the 1:5 ratio to maintain a sufficient amount of QxTh within the composite.

Using 1:5 polymer:GO ratio, an areal capacitance of 186 mF cm^{-2} (372 F cm^{-3}) was achieved at 3,000 deposition cycles which resulted in a 5-μm thick film, while at 1,600 deposition cycles the film was 3.15 μm thick with an areal capacitance of 145 mF cm^{-2} (460 F cm^{-3}), as shown in Figure 2A. These areal capacitance values were obtained from CV characteristics of the composite films as a function of deposition cycles, as shown in Figures S5 and S6. The change in volumetric capacitance with different film thicknesses indicated a gradual change in the distribution of active materials. The rate of film growth was reduced with high deposition cycles, with the film thickness increased by only ∼2 μm between 1,600 and 3,000 cycles. Optimization of the conductive network and increasing the deposition voltage are possible avenues to maintain the deposition rate in the future.

Electrodes with a similar areal capacitance of ∼10 mF cm^{-2} composed of neat polymer, 1:1 and 1:5 polymer:GO were selected for comparative studies, and their electrochemical impedance characteristics are shown in Figures 2B and 2C. The data were fit to an equivalent circuit model (Figure 2C inset) with the best-fit values listed in Table 1. The parameter R_1 represents the electrical resistance of current collectors, and R_i and C_i represent the interfacial resistance and capacitance, respectively,

Please cite this article in press as: Yao et al., Ultrafast high-energy micro-supercapacitors based on open-shell polymer-graphene composites, Cell Reports Physical Science (2022), https://doi.org/10.1016/j.xcrp.2022.100792

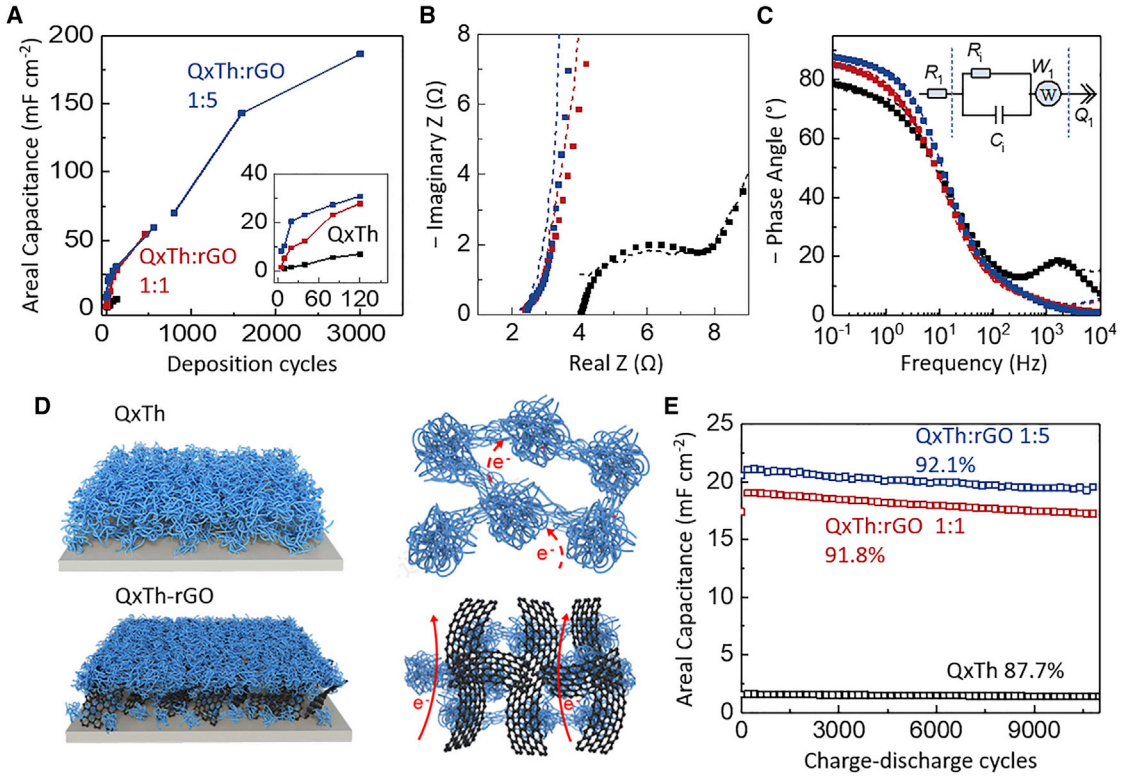

Figure 2. Comparison of different electrode compositions

The same color legend applies to all plots.

(A) Areal capacitance as a function of deposition cycles.

(B) Imaginary impedance versus real impedance, taken on electrodes with an areal capacitance of 10 mF cm^{-2}, biased at −1.5 V versus an Ag/Ag^{+} reference. Measurements are shown in solid symbols, while model fits are represented by dashed lines.

(C) Phase angle versus logarithm of frequency. Inset: equivalent circuit model used for data fits. The parameter definitions are listed in Table 1.

(D) Schematics showing the effects of rGO on the interfacial resistance.

(E) Areal capacitance versus charge-discharge cycles. The charging/discharging current density is 5 mA cm^{-2} for the QxTh electrode, and 35 mA cm^{-2} for the QxTh-rGO electrodes. The current densities were adjusted according to different mass loadings in the electrodes, so that comparisons were across a similar rate of 1.5 V/0.5 s for each full discharge. The samples were films obtained after 80 deposition cycles. The percentage values indicate the capacitance retention after 11,000 cycles.

which indicates the barrier for charge transfer. The Warburg diffusion-controlled resistance W_1 represents the diffusion-controlled resistance, and Q_1 is the constant phase element that models the non-ideal capacitance of the electrode.

In Figure 2B, a prominent difference between the neat polymer and composite electrodes was apparent in the low-frequency regime, where the impedance slopes increased upon rGO addition. For the neat polymer electrode, the impedance data showed a section with a phase angle of 45°, corresponding to W_1. When rGO was incorporated within the electrodes, the W_1 parameters (Table 1) became smaller, implying that electrolyte diffusion was more efficient in the composites. The additional surface area imparted by the rGO leads to shorter diffusion distances for the electrolyte ions to counter-balance charges in the composites.

For the electrode composed solely of polymer, there was a prominent semi-circle region in the impedance plot and a bump in the phase angle at high frequencies above 1 kHz (Figure 2C). These characteristics were attributed to interfacial charge-transfer resistance, originating from either insufficient charge collection at the interface

Please cite this article in press as: Yao et al., Ultrafast high-energy micro-supercapacitors based on open-shell polymer-graphene composites, Cell Reports Physical Science (2022), https://doi.org/10.1016/j.xcrp.2022.100792

Table 1. Fit values to the data taken with electrochemical impedance spectroscopy

	QxTh	1:1 QxTh:rGO	1:5 QxTh:rGO
Deposition cycles	120	20	5
R_1 (Ω)	4.0	2.3	2.4
R_i (Ω)	3.04	0.15	0.34
C_i (mF)	0.04	2.39	2.94
W_1 (mF $s^{-0.5}$)	30.1	8.6	5.2
Q_1 (mF s^{n-1})	2.3	6.1	4.3
n	0.91	0.98	0.99

R_1, resistance of current collectors; R_i, interfacial resistance; C_i, interfacial capacitance; W_1, Warburg diffusion element, with the constant phase angle of 45°; Q_1, constant phase element, with n as the phase angle.

The equivalent circuit model is shown in Figure 2C. The area of each electrode was 0.56 cm^2. The deposition cycles for each material were chosen to obtain similar capacitance (~10 mF cm^{-2}) across all the samples for comparison, and the fitting errors was <10%.

between the current collector and the electrode material, or poor charge conduction across the electrode.[23] The features associated with charge-transfer resistance disappeared upon rGO addition; the composite electrodes exhibited R_i values 10 times lower than the neat polymer film. Electro-deposition of rGO also modified the surface of the current collectors. Neat polymer films were flat, while composite films are nanostructured with additional surface area serving to improve electrical contacts. The rGO also facilitated improved charge transport from the current collector throughout the bulk of the electrode, as depicted in Figure 2D.

In Figure 2E, the capacitance of the electrodes was monitored over 11,000 galvanostatic charge-discharge (GCD) cycles between −2 and −0.5 V (versus Ag/Ag^+) (Figure S7). While the capacitance retention was 87.7% for polymer-based electrodes, it was even higher for polymer-rGO electrodes, with 92% retention for both the 1:1 and 1:5 composites. The cycling stability of the polymer was remarkably better than other n-type polymers which all degrade to well below 80% in far less than a few thousand cycles.[26,30–32,34,35] The improved stability of the polymer-rGO composite could be attributed to rGO networks that withstand repeated expansion and contraction during cycling, while retaining the conductivity necessary to avoid charge trapping in polymer domains.[36]

Device performance

The electrodes fabricated from a 1:5 polymer:GO mixture were used for device fabrication since they displayed the lowest diffusion resistance and the highest cutoff frequency. Supercapacitors were fabricated in either a symmetric or asymmetric configuration as depicted in Figure 3A. In a symmetric supercapacitor, the same redox materials were used for both the cathode and the anode, while an asymmetric device used different materials for each electrode. Since each cathode and anode pair should have an equal charge capacity ($Q = C_A V$) to balance electrode utilization, the number of deposition cycles was tuned to match the areal capacitances C_A of the cathode and anode pair in their respective potential windows. Against an Ag/Ag^+ reference, cathodes operated between −0.5 V and 1 V, while the anodes operated between −2 V and −0.5 V. Thus each electrode spanned a 1.5 V range to give a total device voltage of 3 V.

For symmetric supercapacitors, the composite electrodes operating in the cathodic range showed smaller currents and therefore a lower specific capacitance than in the anodic region (Figure 1B). To compensate for the reduced specific capacitance, the loading mass of the cathode was increased relative to the anode,

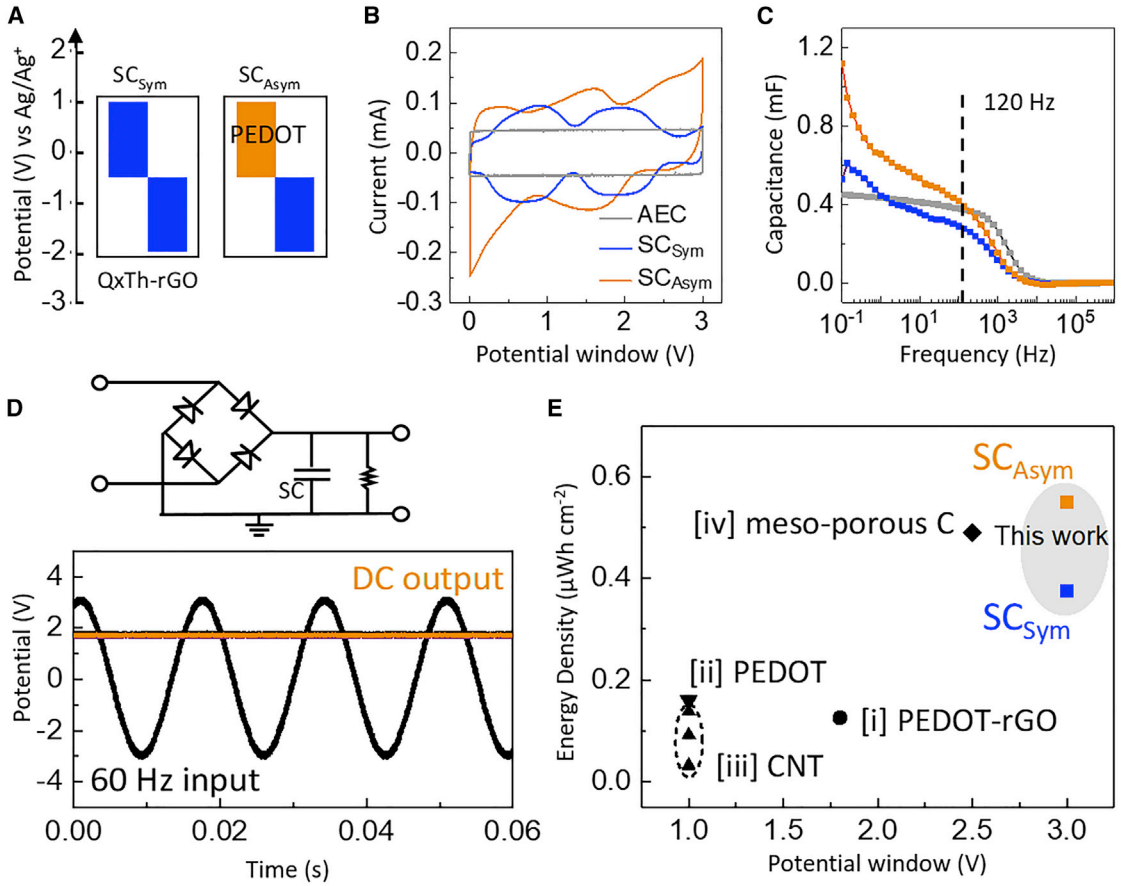

Figure 3. Device characteristics with thin electrodes under AC operation

The same color legend applies to all plots.

(A) Materials of symmetric and asymmetric supercapacitors.

(B) CV scanned at 0.1 V s^{-1}. The AEC was from Nichicon (470 μF at 6.3 V).

(C) Capacitance versus logarithm of frequency, at a bias potential of 3 V, with the corresponding device volumes.

(D) Rectifying circuit and the AC line filtering performance of our supercapacitors.

(E) Energy densities and cell potentials of various supercapacitors operating at 120 Hz. The data are from [i] Wu et al.,[37] [ii] Zhang et al.,[38] [iii] Rangom et al.,[39] and [iv] Yoo et al.[40]

so that the resulting capacitance is equal on both electrodes (details in the section "experimental procedures"). For asymmetric cells, we replaced the QxTh-rGO in the cathode with poly(3,4-ethylenedioxythiophene) (PEDOT)-rGO composites. As seen in Figure S8, the PEDOT-rGO electrodes showed high stability and a porous structure. Compared with symmetric devices, the asymmetric design allowed for similar loading masses between cathode and anode pairs, which increased the overall charge capacity, as evident from the CV characteristics in Figure 3B.

Thin electrodes used in AC line filters

An immediate need in power electronics is to identify a replacement for aluminum electrolytic capacitors (AECs).[41] These bulky AECs are one of the most ubiquitous components in electronic devices and represent a major hurdle toward system miniaturization. Supercapacitors readily provide higher specific capacitance than AECs but are limited in their frequency response. A long-standing goal has been the identification of devices sufficient for rectifying 60-Hz AC line signals, which requires a cutoff frequency beyond 120 Hz. As the surface redox sites and open-pore structures in our composite electrodes facilitated fast electrolyte ion movement, our

supercapacitors could maintain capacitive behaviors to a few hundred hertz. The cutoff frequency, defined as the frequency when the device phase angle dropped to −45°, was 720 Hz for the asymmetric cell (Figure S9C), much higher than typical supercapacitors and batteries that operate at a few hertz. The resistance-capacitance time constant τ_{RC} obtained from the impedance measurement in Figure S9C was 0.43 ms for the asymmetric cell. Figure 3C compares the device capacitances at 120 Hz. When normalized to the packaged device volume (90 μm total thickness, in which the redox composite was 270 nm thick, 1.2 cm^2 in area), the asymmetric redox supercapacitor (516 μF/0.0108 cm^3 = 47.8 mF cm^{-3}) here demonstrated more than 75 times higher volumetric capacitance than a commercial AEC (380 μF/0.6 cm^3 = 0.63 mF cm^{-3}).

Our supercapacitors were integrated in a rectifying circuit to demonstrate an AC line filtering application, as shown in Figure 3D. The input was a ±3 V sinusoidal signal at 60 Hz, to be rectified by the diode bridge to a 120-Hz wave and then low pass filtered by the capacitor into a direct current (DC) output. The DC output was smooth with a magnitude near 2 V; the 1-V drop from the sinusoidal 3V peak was due to the potential drop across the diodes. There was only 0.04 V negligible difference between using an AEC versus our redox supercapacitors, attributed to the smaller phase angle (75.5° at 120 Hz) in the supercapacitors (~8° smaller than AEC as shown in Figure S9C). While there are prior supercapacitors with higher cutoff frequency, they are limited by a small potential window (0.8–1.6 V).[37–40] The supercapacitors in this work achieved a significantly higher potential window and energy density than prior electrochemical devices made for AC line filters, as seen in Figure 3E. Compared with other fast supercapacitors that are limited in their voltage, the 3 V operation range decreases the number of layers that need to be connected in series to reach a desired voltage rating. Consequently, the device stack will be considerably more compact with reduced series resistance for power applications.

Thick electrodes enabling simultaneous high power and high energy densities

The symmetric and asymmetric electrodes were fabricated with thicknesses of <200 nm to demonstrate their utility in 120-Hz applications. For other use cases, such as energy storage buffers in power trains or power supplies for wireless sensors, thicker electrodes that provide increased energy capacities are required. As the electrode thickness was increased, the equivalent series resistance (ESR) became large, impeding operation at high rates. With the new redox composites detailed in this work, we examined the possibility of increasing the energy density while keeping ESR low through the conductive rGO networks. During the fabrication of thick electrodes (~1.6–3.2 μm), we annealed the films at 200°C for 30 min midway through the deposition process, which resulted in improved film conductivity (Figure S5A).

For the asymmetric supercapacitor using PEDOT-rGO as the cathode and QxTh-rGO as the anode (Figure 4A), the GCD characteristics showed the device charging/discharging within 3 V at 160 mA cm^{-2}, which yielded a power density of 227 mW cm^{-2} (114.6 W cm^{-3}). Such a high-power delivery has not been achieved for any materials combination as depicted in the Ragone plot in Figure 4B. For comparison purposes, the next highest-performing alternative is carbide-derived carbon.[42] However, these devices show a lower energy density than the ones in this work when power delivery exceeds 30 mW cm^{-2} (15.2 W cm^{-3}). Previously reported organic supercapacitors result in performance that is an order of magnitude lower than demonstrated here.

Please cite this article in press as: Yao et al., Ultrafast high-energy micro-supercapacitors based on open-shell polymer-graphene composites, Cell Reports Physical Science (2022), https://doi.org/10.1016/j.xcrp.2022.100792

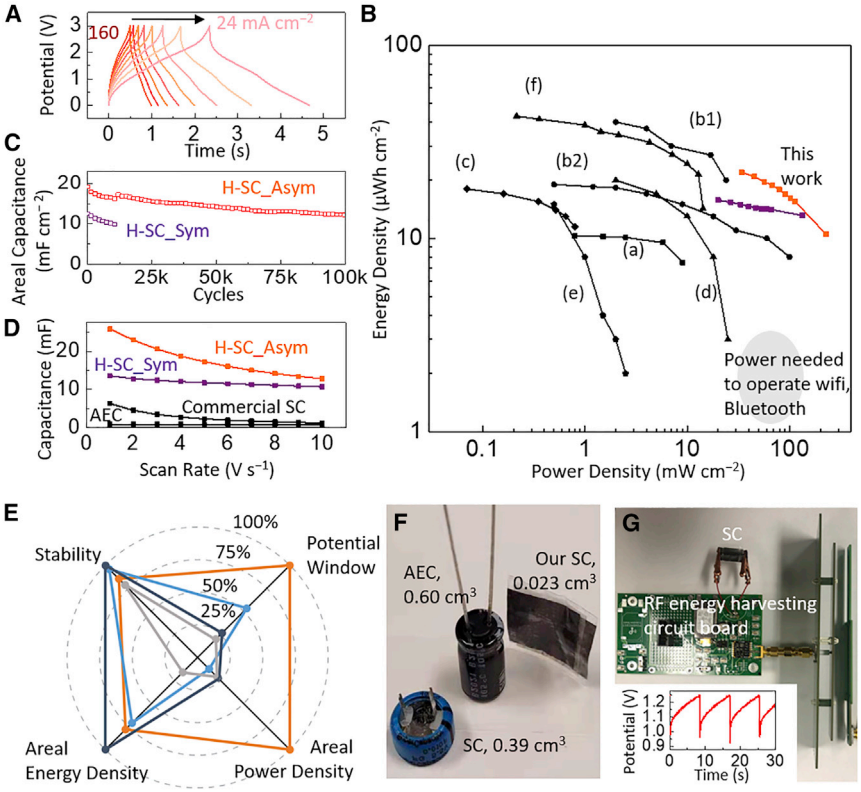

Figure 4. Characterization of power and energy densities of devices with thick electrodes

(A) GCD curves of the asymmetric supercapacitor, at current densities of 160 mA cm^{-2} and 80–24 mA cm^{-2} in decrements of 8 mA cm^{-2}.

(B) Energy density versus power density of state-of-the-art supercapacitors: (a) vanadium nitride[43]; (b1, b2) carbide-derived carbon[42]; (c) CuOH@FeOOH nanotubes[44]; (d) onion-like carbon[45]; (e) MoOx[46]; (f) MnO_2-Graphene.[11]

(C) Areal capacitance versus charge-discharge cycles. Due to different mass loadings in the devices, the current densities were adjusted to 15 mA cm^{-2} (Sym) and 20 mA cm^{-2} (Asym) so that comparisons were across the same rate of 3 V/2.5 s for each full discharge.

(D) Capacitance as a function of scan rate for our supercapacitors, an aluminum electrolytic capacitor (AEC: Nichicon B01DYJEH22), and a commercial activated carbon supercapacitor (SC: KEMET FG0H103ZF).

(E) Comparison between state-of-the-art devices and asymmetric device (orange data) in this work. Dark blue, Huang et al.[42]; light blue, El-Kady et al.[11]; gray, Hongwei et al.[46] Each metric axis was normalized to the highest value shown in Table S3.

(F) Photograph of the devices in (D).

(G) Photograph of an RF energy harvesting circuit with our symmetric supercapacitor as the energy storage unit. The inset shows the charging and discharging cycles.

Conventional electrochemical energy storage devices are slow and rely on bulky AEC buffers to facilitate sufficient power delivery. Our devices directly deliver high power without AECs for common applications such as radio-frequency (RF) communication. The energy storage density reached 21.9 μWh cm^{-2} (11 mWh cm^{-3}) at a discharge power of 36 mW cm^{-2} (18.2 W cm^{-3}). This energy capacity meets the needs of a growing number of sensor electronics that are designed to consume low energy on the order of tens of μWh cm^{-2}.[25] This capacity allows these supercapacitors to serve as a stand-alone energy supply and offers an alternative to battery technologies limited by short cycle lifetime.

The devices were fully charged and discharged for 11,000 redox cycles, as shown in Figure 4C, with a capacitance retention of 84.1% and 77.5% for the asymmetric and

Table 2. Capacitance and energy density comparisons, including the volume of package materials

	AEC (Nichicon B01DYJEH22)	Activated C SC (KEMET FG0H103ZF)	H-SC_ Sym	H-SC_ Asym
Capacitance* (mF) at 1 V s^{-1}	0.94	6.35	13.6	25.8
Volume (cm^3)	0.60	0.39	0.023	0.023
Potential window (V)	6.3	12	3	3
Volumetric capacitance (mF cm^{-3})	1.5	16.3	591.3	1121.7
Volumetric energy density (μWh cm^{-3})	8.3	325.1	739	1402

*Here, the parameters are measured at the rate of 1 V s^{-1}, slower than the 120-Hz conditions (3V/8.3 ms = 360 V s^{-1}) in Figure 3 and therefore the values are different between these two cases.

symmetric cells, respectively. The comparison of cycling stability among pseudocapacitive devices is shown in Table S2. Note that our cycling condition was across 3 V, and, if the potential was decreased to 1.5 V, capacitance retention would improve to 92%. After 100,000 cycles of 3 V operation, the asymmetric device maintained 63% of its initial capacitance, and the reduced value would still be better than the initial volumetric capacitance of commercial devices in Table 2. Our symmetric cell showed a smaller areal capacitance and slightly reduced capacitance retention than the asymmetric device; however, the symmetric cell was less adversely affected by an increase in the scan rate from 1 V s^{-1} to 10 V s^{-1} (Figures 4D and S10, S11 and S12). The low dependence on scan rates indicates that the redox kinetics in QxTh-rGO composite materials are fast and do not limit the charge/discharge rate. For the asymmetric cell, the PEDOT-rGO cathode was more resistive than QxTh polymer-rGO anode, leading to a larger drop in capacitance upon increasing the scan rates. On account of its high degree of charge delocalization, the open-shell QxTh polymer-rGO composite is shown to be an excellent anode that facilitates fast kinetics and high redox stability using a large potential window that has eluded other n-type Faradaic electrodes.

The radar plot in Figure 4E compares our asymmetric device with three other state-of-the-art supercapacitors. The device in this work featured much higher power density and potential window than the others while showing similar values in terms of stability and energy density, as listed in Table S3. The asymmetric device displayed better kinetics and a volumetric energy density 4.3-fold higher than commercial activated carbon supercapacitors (Table 2 and Figure 4F). These results are consistent with high storage capacity, high power, and outstanding stability, offering a potential replacement for AECs or batteries within miniaturized and low-power electronics. Lastly, we integrated our symmetric supercapacitor with an RF energy harvesting board, in which the cell was the sole energy storage component used to power the wireless circuit. The resulting charge and discharge cycles of the supercapacitors are shown in Figure 4G, demonstrating the potential of using our redox supercapacitors as energy storage solutions for wireless sensors.

In summary, this work presents a new design that simultaneously advanced the three key metrics of power, energy, and stability in redox supercapacitors. This was accomplished through the synergistic combination of novel open-shell polymers that demonstrate enhanced delocalization in their redox states with rGO and the utilization of low-cost electro-deposition methodologies. The micrometer-thick electrodes maintained fast kinetics through the conductive rGO framework and showed high energy density on account of the conjugated polymer, which enabled operation with a large potential window of 3 V. Impedance analyses and modeling demonstrated that optimization of the polymer-to-rGO ratio

Please cite this article in press as: Yao et al., Ultrafast high-energy micro-supercapacitors based on open-shell polymer-graphene composites, Cell Reports Physical Science (2022), https://doi.org/10.1016/j.xcrp.2022.100792

improved interfacial charge-transfer resistance and diffusion-controlled resistance. With a high degree of electronic delocalization and mechanical flexibility in the composite electrodes, our supercapacitors exhibited exceptional capacitance retention of 84% in supercapacitors after 11,000 full redox cycles, offering the critical benefit of long cycle life to significantly reduce maintenance and replacement costs.

For use case studies, we successfully applied our redox supercapacitors in a 120-Hz filter circuit. The superior volumetric capacitance and energy density make them an attractive alternative to bulky AECs. As the active material loading was increased, the device response decreased below 120 Hz, but the power density remained outstanding. These devices demonstrated charge/discharge power of 227 mW cm^{-2} (114.6 W cm^{-3}) with an energy density of 10.5 μWh cm^{-2} (5.3 mWh cm^{-3}). At a power rate of 36 mW cm^{-2} (18.2 W cm^{-3}), the asymmetric device provided an energy density of 21.9 μWh cm^{-2} (11 mWh cm^{-3}). Such high-power and high-energy performance showcased the potential of this class of redox supercapacitors to serve as compact, fast-charging power supplies that are well suited to meeting the rising demands of wireless electronics.

EXPERIMENTAL PROCEDURES

Resource availability

Lead contact

Further information and requests for resources and procedures should be directed to the lead contact, Dr. Tse Nga Ng (tnn046@ucsd.edu).

Materials availability

All unique surfaces generated in this study are available from the lead contact without restriction.

Data and code availability

All of the data supporting the findings of this study are presented within the article and supplemental information. All other data are available from the lead contact upon reasonable request.

Electrode preparation

QxTh-rGO electrodes

The cathodic electro-polymerization process was conducted in a three-electrode configuration, with a graphite foil (conductivity, ~16,000 S cm^{-1}; thickness, 16 μm; from Emitac New Material Technology) as the working electrode, an activated carbon cloth for the counter electrode, and an Ag/Ag^+ reference electrode. The process was conducted inside a nitrogen-filled glove box. The chemicals purchased from Sigma-Aldrich were used as received. The synthetic procedure for the QxTh monomers is described in the supplemental experimental procedures. For the electro-deposition of QxTh, a mixed solvent of dichloromethane (DCM) and propylene carbonate (PC) in a 2:3 volume ratio was used to dissolve QxTh to give a concentration of 1 mg mL^{-1} with tetrabutylammonium hexafluorophosphate ($TBAPF_6$) at a concentration of 0.1 M. The applied voltage on the working electrode was cyclically scanned between −0.5 and 0.8 V (versus Ag/Ag^+) at 50 mV s^{-1} to polymerize the monomers. For the deposition of rGO, either 1 or 5 mg mL^{-1} GO prepared by a modified Hummers' method[43] was added to the same electrolyte as used for QxTh, and the deposition potential was held at –2 V for 5 s. The deposition proceeded by repeating the deposition voltage waveform. After deposition, the electrodes were annealed at 200°C for 30 min and then scanned between −0.5

Please cite this article in press as: Yao et al., Ultrafast high-energy micro-supercapacitors based on open-shell polymer-graphene composites, Cell Reports Physical Science (2022), https://doi.org/10.1016/j.xcrp.2022.100792

and 1 V in the electrolyte (0.1 M $TBAPF_6$ in DCM:PC) for 20 cycles to eliminate residual monomers in the films.

PEDOT-rGO electrodes

This electrode was prepared using the same electro-polymerization method as for QxTh-rGO, except that the monomer was 3,4-ethylenedioxythiophene (EDOT) at 2 mg mL^{-1} concentration and GO was at 5 mg mL^{-1}. The waveform to polymerize EDOT was set between −0.5 and 1 V scanning at 50 mV s^{-1}, while the rGO formation potential was kept at –2 V for 5 s.

Device fabrication

The supercapacitors were sandwich structures, as shown in Figure S7. To balance charge capacity in the electrode pairs, the number of deposition cycles was adjusted so that the cathode and anode reach equal areal capacitance C_A. The electrodes were isolated by a cellulose paper separator (30 μm, Japan NKK and TF4030), and the device electrolyte was 1 M tetraethylammonium tetrafluoroborate ($TEABF_4$) in acetonitrile. Polyethylene terephthalate (PET) films of 25-μm thickness were used for packaging devices, for which the PET pouch was formed by pressing the edges with a heat sealer at 60°C for 5 s.

In Figure 3, the anodes were fabricated with five deposition cycles in a 1:5 QxTh:GO solution in above. For the SC_Sym device, the cathode was made using the same materials as the anode, but the cathode was processed with 10 deposition cycles in order to match the C_A of the anode. The film thickness was roughly 90 nm for the anode and 180 nm for the cathode. For the SC_Asym device, the cathode was a PEDOT-rGO electrode with a mass loading of 2.49 mg cm^{-2} (calculated based on specific capacitance and areal capacitance).

In Figure 4, the anodes with high energy densities were fabricated with 800 deposition cycles in a 1:5 QxTh:GO solution. Due to the increase in thickness, the deposition was paused midway (at the 400^{th} cycle in an 800-cycles deposition, or at the 500^{th} cycle in a 1,000-cycle deposition, and so forth) to add an annealing step of 200°C for 30 min. This served to improve the film conductivity and maintain the deposition efficiency. A new monomer and electrolyte solution were subsequently used for the second half of the electro-deposition process. For the H-SC_Sym device, the cathode was made with QxTh-rGO deposited using 1,600 cycles. The film thicknesses were roughly 1.6 μm for the anode and 3.15 μm for the cathode. For the H-SC_Asym device, the cathode was PEDOT-rGO deposited using 1,000 cycles.

Device characterization

The morphologies of electro-deposited films were imaged on a Field Electron and Ion Company (FEI) scanning electron microscope at 5 kV. The thicknesses of the deposited films were measured using SEM. The SEM images of the electrode before and after 100,000 full redox cycles are included in Figure S12. The pore size of the electrode appeared larger than 100 nm in SEM images. The pores provided diffusion channels for electrolyte ions but were not a significant contributor to electric double-layer capacitance (EDLC). In Figure S13, the Brunauer-Emmett-Teller analysis of the 1:5 QxTh:rGO film at 560 deposition cycles showed that the surface area was 4.7 m^2 g^{-1}, much lower than EDLC electrodes like activated carbon, in agreement with our CV data that most of the capacitance contribution come from redox and not from EDLC.

Electrochemical measurements were carried out using a Bio-Logic SP-200 potentiostat. For individual electrodes, the samples were set in a Swagelok cell in the three-electrode configuration. The electrolyte was 0.5 M $TEABF_4$ in PC, and measurements were carried out inside a nitrogen-filled glove box. For the sealed supercapacitors, the samples were measured in two-electrode configuration in ambient conditions.

The potential windows of CV and GCD measurements were conducted at a scan rate of 0.1 V s^{-1} from −2 V to −0.5 V for anodes and −0.5 to 1 V for cathodes, with Ag/Ag^+ as the reference. For packaged cells, the voltage scan was between 0 V and 3 V. As the electrodes were thin films, we reported parameters normalized over the device area, which typically ranged from 1.25 to 2.25 cm^2. The areal capacitance was calculated from the relationship $C_A = J \cdot t/V$, where J is the current density to be integrated over the scan time t, and V is the scan voltage window. The thicknesses of substrates (graphite foil, 15 μm), separator (cellulose paper, 30 μm), and encapsulation PET film (25 μm) were much higher than the active materials (90 nm–3.15 μm). Hence, the cell thickness was ∼60–68 μm ((2 × 15 + 30 μm) + active materials) for cell volume calculations, excluding the separator thickness.

Electrochemical impedance spectroscopy was performed at various DC biases, with an AC amplitude of 10 mV and frequencies ranging from 0.1 Hz to 1 MHz. Fittings to the equivalent circuit model were conducted by the Z fit function in the software Zview 2. The impedance change with frequency f was $Z(f) = W1 \cdot (2)^{0.5}(i2\pi f)^{-0.5}$ for the Warburg element $W1$, and $Z(f) = (1/Q1)(j2\pi f)^{-n}$ for the constant phase element $Q1$. Capacitance retention was calculated by dividing the current capacitance value by the initial value. The energy density of a supercapacitor is calculated by the equation $E = CV^2/2$, and the power density is determined according to the equation $P = E/\Delta t = JV/2$, in which Δt is the discharge time.[44,47]

For the AC line filter in Figure 3D, the resistor value is 10 kΩ, and the turn-on voltage is ∼1 V for the diodes (MDB10S, ON Semiconductor) in the rectifier bridge. For the demonstration in Figure 4F, the RF energy-harvesting circuit was from the 915-MHz P2110 Evaluation Board (Powercast). This board converted RF energy into DC power,[48] and we replaced the onboard storage capacitor with our own H-SC-Sym supercapacitor. The voltage on the supercapacitor was monitored with an oscilloscope.

DFT calculations

DFT calculations at the unrestricted (U)B3LYP/6-31G** level of the theory were carried out on oligomers with an increasing number of repeat units (n) in order to understand the evolution of the electronic structure and relate it to the supercapacitor performance. The procedure is described in the supplemental experimental procedures. Broken-symmetry (BS) singlet-state calculations were started with a restricted wave-function. The diradical index (y) was calculated using both Highest Occupied Natural Orbital (HONO) and Lowest Unoccupied Natural Orbital (LUNO) occupation number and Yamaguchi's formula. The optimized octamer geometry was subjected to single-point calculations to identify the orbital topology using the electron and spin density distributions along with the MESP maps upon varying the redox states of the polymer. The electron density isosurface was set to 0.001 atomic units for the generation of MESP surfaces.

SUPPLEMENTAL INFORMATION

Supplemental information can be found online at https://doi.org/10.1016/j.xcrp.2022.100792.

ACKNOWLEDGMENTS

The authors L.Y., J.L., and T.N.N. are grateful for the support from National Science Foundation PFI-2120103 and MCA-2120701. Part of the work was performed at the San Diego Nanotechnology Infrastructure of UCSD, which is supported by NSF ECCS-1542148. The work performed at The University of Southern Mississippi was made possible through the Air Force Office of Scientific Research (AFOSR) with support provided by the Organic Materials Chemistry Program (grant FA9550-20-1-0353) and the National Science Foundation (OIA-1757220). DFT calculations were performed at USM using the High Performance Computational (HPC) Cluster supported by the NSF (OAC-1626217).

AUTHOR CONTRIBUTIONS

L.Y. carried out the electrochemical polymerization, device fabrication, and materials/device characterization. J.L. conducted the RF energy harvesting experiments. N.E. and J.D.A. designed the polymer and synthesized the monomer. P.M. performed DFT calculations. D.J.A. and K.S.M. characterized the open-shell properties of the polymer. K.W. contributed to the design and optimization of electro-polymerization process. T.N.N. conceived the idea and supervised the project.

DECLARATION OF INTERESTS

The authors declare no completing interests.

Received: September 17, 2021
Revised: January 10, 2022
Accepted: February 9, 2022
Published: March 2, 2022

REFERENCES

1. Fleischmann, S., Mitchell, J.B., Wang, R., Zhan, C., Jiang, D., Presser, V., and Augustyn, V. (2020). Pseudocapacitance: from fundamental understanding to high power energy storage materials. Chem. Rev. *120*, 6738–6782.
2. Simon, P., and Gogotsi, Y. (2020). Perspectives for electrochemical capacitors and related devices. Nat. Mater. *19*, 1151–1163.
3. Choi, C., Ashby, D.S., Butts, D.M., DeBlock, R.H., Wei, Q., Lau, J., and Dunn, B. (2020). Achieving high energy density and high power density with pseudocapacitive materials. Nat. Rev. Mater. *5*, 5–19.
4. Fan, Z., Islam, N., and Bayne, S.B. (2017). Towards kilohertz electrochemical capacitors for filtering and pulse energy harvesting. Nano Energy *39*, 306–320.
5. Miller, J.R., Outlaw, R.A., and Holloway, B.C. (2010). Graphene double-layer capacitor with ac line-filtering performance. Science *329*, 1637–1639.
6. Lethien, C., Le Bideau, J., and Brousse, T. (2019). Challenges and prospects of 3D micro-supercapacitors for powering the internet of things. Energy Environ. Sci. *12*, 96–115.
7. Adu-Manu, K.S., Adam, N., Tapparello, C., Ayatollahi, H., and Heinzelman, W. (2018). Energy-harvesting wireless sensor networks (EH-WSNs): a review. ACM Trans. Sen. Netw. *14*, 10.
8. Li, X., Li, H., Fan, X., Shi, X., and Liang, J. (2020). 3D-Printed stretchable micro-supercapacitor with remarkable areal performance. Adv. Energy Mater. *10*, 1903794.
9. Wu, Z.-S., Parvez, K., Li, S., Yang, S., Liu, Z., Liu, S., Feng, X., and Müllen, K. (2015). Alternating stacked graphene-conducting polymer compact films with ultrahigh areal and volumetric capacitances for high-energy micro-supercapacitors. Adv. Mater. *27*, 4054–4061.
10. Ferris, A., Garbarino, S., Guay, D., and Pech, D. (2015). 3D RuO2 microsupercapacitors with remarkable areal energy. Adv. Mater. *27*, 6625–6629.
11. El-Kady, M.F., Ihns, M., Li, M., Hwang, J.Y., Mousavi, M.F., Chaney, L., Lech, A.T., and Kaner, R.B. (2015). Engineering three-dimensional hybrid supercapacitors and microsupercapacitors for high-performance integrated energy storage. Proc. Natl. Acad. Sci. U SA *112*, 4233–4238.
12. Yue, Y., Liu, N., Ma, Y., Wang, S., Liu, W., Luo, C., Zhang, H., Cheng, F., Rao, J., Hu, X., et al. (2018). Highly self-healable 3D microsupercapacitor with MXene–graphene composite aerogel. ACS Nano *12*, 4224–4232.
13. Nomura, K., Nishihara, H., Kobayashi, N., Asada, T., and Kyotani, T. (2019). 4.4 V supercapacitors based on super-stable mesoporous carbon sheet made of edge-free graphene walls. Energy Environ. Sci. *12*, 1542–1549.
14. Jiang, H., Lee, P.S., and Li, C. (2013). 3D carbon based nanostructures for advanced supercapacitors. Energy Environ. Sci. *6*, 41–53.
15. Xia, Y., Mathis, T.S., Zhao, M., Anasori, B., Dang, A., Zhou, Z., Cho, H., Gogotsi, Y., and Yang, S. (2018). Thickness-independent capacitance of vertically aligned liquid-crystalline MXenes. Nature *6*, 409–412.
16. Liang, J., Mondal, A.K., Wang, D.-W., and Iacopi, F. (2019). Graphene-based planar microsupercapacitors: recent advances and future challenges. Adv. Mater. Technol. *4*, 1800200.
17. Li, Z., Gadipelli, S., Li, H., Howard, C.A., Brett, D.J.L., Shearing, P.R., Guo, Z., Parkin, I.P., and Li, F. (2020). Tuning the interlayer spacing of graphene laminate films for efficient pore utilization towards compact capacitive energy storage. Nat. Energy *5*, 160–168.
18. Kamboj, N., Purkait, T., Das, M., Sarkar, S., Hazra, K.S., and Dey, R.S. (2019). Ultralong cycle life and outstanding capacitive performance of a 10.8 v metal free micro-supercapacitor with highly conducting and robust laser-irradiated graphene for an integrated storage device. Energy Environ. Sci. *12*, 2507–2517.

19. Muench, S., Wild, A., Friebe, C., Häupler, B., Janoschka, T., and Schubert, U.S. (2016). Polymer-based organic batteries. Chem. Rev. *116*, 9438–9484.

20. Lu, Y., and Chen, J. (2020). Prospects of organic electrode materials for practical lithium batteries. Nat. Rev. Chem. *4*, 127–142.

21. Wang, K., Huang, L., Eedugurala, N., Zhang, S., Sabuj, M.A., Rai, N., Gu, X., Azoulay, J.D., and Ng, T.N. (2019). Wide potential window supercapacitors using open-shell donor–acceptor conjugated polymers with stable N-doped states. Adv. Energy Mater. 1902806.

22. Huang, L., Eedugurala, N., Benasco, A., Zhang, S., Mayer, K.S., Adams, D.J., Fowler, B., Lockart, M.M., Saghayezhian, M., Tahir, H., et al. (2020). Open-shell donor–acceptor conjugated polymers with high electrical conductivity. Adv. Funct. Mater. *30*, 1909805.

23. Eftekhari, A. (2018). The mechanism of ultrafast supercapacitors. J. Mater. Chem. A. *6*, 2866–2876.

24. Toor, A., Wen, A., Maksimovic, F., Gaikwad, A.M., Pister, K.S.J., and Arias, A.C. (2021). Stencil-printed Lithium-ion micro batteries for IoT applications. Nano Energy *82*, 105666.

25. Shen, C., Xu, S., Xie, Y., Sanghadasa, M., Wang, X., and Lin, L. (2017). A review of on-chip micro supercapacitors for integrated self-powering systems. J. Microelectromech. Syst. *26*, 949–965.

26. Zhang, H., Yao, M., Wei, J., Zhang, Y., Zhang, S., Gao, Y., Li, J., Lu, P., Yang, B., and Ma, Y. (2017). Stable p/n-Dopable conducting redox polymers for high-voltage pseudocapacitor electrode materials: structure–performance relationship and detailed investigation into charge-trapping effect. Adv. Energy Mater. *7*, 1701063.

27. Liang, Y., Chen, Z., Jing, Y., Rong, Y., Facchetti, A., and Yao, Y. (2015). Heavily n-dopable π-conjugated redox polymers with ultrafast energy storage capability. J. Am. Chem. Soc. *137*, 4956–4959.

28. Wang, S., Li, F., Easley, A.D., and Lutkenhaus, J.L. (2019). Real-time insight into the doping mechanism of redox-active organic radical polymers. Nat. Mater. *18*, 69–75.

29. Sung, S.H., Savoie, B.M., Boudouris, B.W., Joo, Y., and Agarkar, V. (2018). A nonconjugated radical polymer glass with high electrical conductivity. Science *359*, 1391–1395.

30. Bryan, A.M., Santino, L.M., Lu, Y., Acharya, S., and D'Arcy, J.M. (2016). Conducting polymers for pseudocapacitive energy storage. Chem. Mater. *28*, 5989–5998.

31. Schon, T.B., McAllister, B.T., Li, P.F., and Seferos, D.S. (2016). The rise of organic electrode materials for energy storage. Chem. Soc. Rev. *45*, 6345–6404.

32. Shao, Y., El-Kady, M.F., Sun, J., Li, Y., Zhang, Q., Zhu, M., Wang, H., Dunn, B., and Kaner, R.B. (2018). Design and mechanisms of asymmetric supercapacitors. Chem. Rev. *118*, 9233–9280.

33. Ji, H., Zhao, X., Qiao, Z., Jung, J., Zhu, Y., Lu, Y., Zhang, L.L., MacDonald, A.H., and Ruoff, R.S. (2014). Capacitance of carbon-based electrical double-layer capacitors. Nat. Commun. *5*, 3317.

34. McAllister, B.T., Schon, T.B., DiCarmine, P.M., and Seferos, D.S. (2017). A study of fused-ring thieno[3,4-: E] pyrazine polymers as n-type materials for organic supercapacitors. Polym. Chem. *8*, 5194–5202.

35. Schon, T.B., Dicarmine, P.M., and Seferos, D.S. (2014). Polyfullerene electrodes for high power supercapacitors. Adv. Energy Mater. *4*, 1301509.

36. Zhang, H., Tang, X., Zhao, D., Zheng, N., Huang, L., Sun, T., Gu, C., and Ma, Y. (2020). Suppressing charge trapping effect in ambipolar conducting polymer with vertically standing graphene as the composite electrode for high performance supercapacitor. Energy Storage Mater *29*, 281–286.

37. Zhang, M., Zhou, Q., Chen, J., Yu, X., Huang, L., Li, Y., Li, C., and Shi, G. (2016). An ultrahigh-rate electrochemical capacitor based on solution-processed highly conductive PEDOT:PSS films for AC line-filtering. Energy Environ. Sci. *9*, 2005–2010.

38. Rangom, Y., Tang, X., Shirley), and Nazar, L.F. (2015). Carbon nanotube-based supercapacitors with excellent ac line filtering and rate capability via improved interfacial impedance. ACS Nano *9*, 7248–7255.

39. Yoo, Y., Kim, M.-S., Kim, J.-K., Kim, Y.S., and Kim, W. (2016). Fast-response supercapacitors with graphitic ordered mesoporous carbons and carbon nanotubes for AC line filtering. J. Mater. Chem. A. *4*, 5062–5068.

40. Gund, G.S., Park, J.H., Harpalsinh, R., Kota, M., Shin, J.H., Kim, T.I., Gogotsi, Y., and Park, H.S. (2019). MXene/polymer hybrid materials for flexible AC-filtering electrochemical capacitors. Joule *3*, 164–176.

41. Wu, M., Chi, F., Geng, H., Ma, H., Zhang, M., Gao, T., Li, C., and Qu, L. (2019). Arbitrary waveform AC line filtering applicable to hundreds of volts based on aqueous electrochemical capacitors. Nat. Commun. *10*, 2855.

42. Huang, P., Lethien, C., Pinaud, S., Brousse, K., Laloo, R., Turq, V., Respaud, M., Demortière, A., Daffos, B., Taberna, P.L., et al. (2016). On-chip and freestanding elastic carbon films for micro-supercapacitors. Science *351*, 691–695.

43. Choi, C., Robert, K., Whang, G., Roussel, P., Lethien, C., and Dunn, B. (2021). Photopatternable hydroxide ion electrolyte for solid-state micro-supercapacitors. Joule *5*, 2466–2478.

44. Xie, J.-Q., Ji, Y.-Q., Kang, J.-H., Sheng, J.-L., Mao, D.-S., Fu, X.-Z., Sun, R., and Wong, C.-P. (2019). In situ growth of Cu(OH)2@FeOOH nanotube arrays on catalytically deposited Cu current collector patterns for high-performance flexible in-plane micro-sized energy storage devices. Energy Environ. Sci. *12*, 194–205.

45. Pech, D., Brunet, M., Durou, H., Huang, P., Mochalin, V., Gogotsi, Y., Taberna, P.-L., and Simon, P. (2010). Ultrahigh-power micrometre-sized supercapacitors based on onion-like carbon. Nat. Nanotechnol. *5*, 651–654.

46. Sheng, H., Zhou, J., Li, B., He, Y., Zhang, X., Liang, J., et al. (2021). A thin, deformable, high-performance supercapacitor implant that can be biodegraded and bioabsorbed within an animal body. Sci. Adv. *7*, eabe3097.

47. Zhang, S., and Pan, N. (2015). Supercapacitors performance evaluation. Adv. Energy Mater. *5*, 1401401.

48. Wang, K., Yao, L., Jahon, M., Liu, J., Gonzalez, M., Liu, P., Leung, V., Zhang, X., and Ng, T.N. (2020). Ion-exchange separators suppressing self-discharge in polymeric supercapacitors. ACS Energy Lett *5*, 3276–3284.